Analyzing the Effect of High-k Dielectric-Mediated Doping on Contact Resistance in Top-Gated Monolayer MoS_2 Transistors

Abdullah Alharbi, *Member, IEEE*, and Davood Shahrjerdi, *Senior Member, IEEE*

(Invited Paper)

***Abstract*— A scalable process that can yield low-resistance contacts to transition metal dichalcogenides is crucial for realizing a viable device technology from these materials. Here, we systematically examine the effect of high-k dielectric-mediated doping on key device metrics including contact resistance and carrier mobility. Specifically, we use top-gated transistors from monolayer MoS_2 as a test vehicle and vary the MoS_2 doping level by adjusting the amount of oxygen vacancies in the HfO_x gate dielectric. To understand the effect of doping on the contact resistance, from a fundamental standpoint, we first estimate the doping level in monolayer MoS_2. The results of our device studies quantitatively show that the reduction in contact resistance with an increase in doping is due to the doping-induced lowering of the Schottky barrier height (SBH) at the metal–semiconductor interface. Furthermore, our temperature-dependent measurements reveal that a mixture of thermionic and field emissions, even at high carrier densities, dominates carrier conduction at the contact. While our study reveals the effectiveness of dielectric-induced doping in lowering SBH, it suggests that a further reduction of SBH using alternative methods is necessary for achieving an ohmic-like contact to monolayer MoS_2.**

***Index Terms*— Contact engineering, contact resistance, doping, MoS_2, temperature-dependent, transistors, transition metal dichalcogenide (TMD), transport.**

Manuscript received May 1, 2018; revised June 25, 2018; accepted August 15, 2018. Date of publication September 6, 2018; date of current version September 20, 2018. This work was supported in part by NSF under Award #1638598, in part by the U.S. Army Research Office under Award #W911NF-16-1-0301, in part by the Center for Functional Nanomaterials, which is a U.S. DOE Office of Science Facility, at the Brookhaven National Laboratory under Contract DE-SC0012704. The review of this paper was arranged by Editor J. T. Teherani. *(Corresponding author: Davood Shahrjerdi.)*

A. Alharbi is with the Department of Electrical and Computer Engineering, New York University, Brooklyn, NY 11201 USA, and also with the National Center for Nanotechnology, King Abdulaziz City for Science and Technology, Riyadh 11442-6086, Saudi Arabia (e-mail: alharbi@nyu.edu).

D. Shahrjerdi is with the Department of Electrical and Computer Engineering, New York University, Brooklyn, NY 11201 USA, and also with the Center for Quantum Phenomena, Department of Physics, New York University, New York, NY 10003 USA (e-mail: davood@nyu.edu).

Color versions of one or more of the figures in this paper are available online at http://ieeexplore.ieee.org.

Digital Object Identifier 10.1109/TED.2018.2866772

I. Introduction

LAYERED transition metal dichalcogenides (TMDs) are promising for next generation of electronic and optoelectronic device applications. They offer a range of unique physical properties including dependence of their bandgap size and type on the number of layers [1], strong spin–orbit coupling [2], and strong exciton binding energy [3]. However, the formation of low-resistance contacts using a technologically viable approach remains a difficult challenge.

Past studies on contact engineering of TMDs can be classified into three general categories: 1) work function engineering [4]–[7]; 2) chemical and electrical doping of the TMDs [8]–[11]; and 3) interface engineering by: a) inserting a tunnel barrier such as monolayer h-BN [12]–[14] between the metal electrode and the TMD or b) contact formation under ultrahigh vacuum conditions [15]. Among these, the dielectric-mediated doping of TMDs [9], [16] offers a stable process with a potential for contact engineering of TMD devices on a technologically relevant scale. The utility of this technique has been experimentally demonstrated using a variety of high-k dielectrics [9], [16]–[18]. For example, a report by Rai *et al.* [17] indicates that the oxygen vacancy in TiO_x can induce doping in monolayer MoS_2, yielding desirable effects on key device metrics such as the reduction in the contact resistance and increase in the carrier mobility [9]. Despite the significant advances on contact engineering based on dielectric-mediated doping, until now, no study has systematically investigated the effect of different doping levels on the contact resistance and the underlying carrier conduction mechanism at the contacts. Addressing this question is the subject of this paper.

Here, we systematically investigate the effects of dielectric-mediated doping of the transistor channel, specifically at regions in vicinity of source/drain electrodes, on the contact resistance of monolayer MoS_2 transistors. We induced n-type doping in monolayer MoS_2 films using a substoichiometric HfO_x layer, which simultaneously acts as the gate dielectric in our top-gated devices. By systematically varying the stoichiometric oxygen content of the HfO_x layer, we produced multiple device samples with different doping

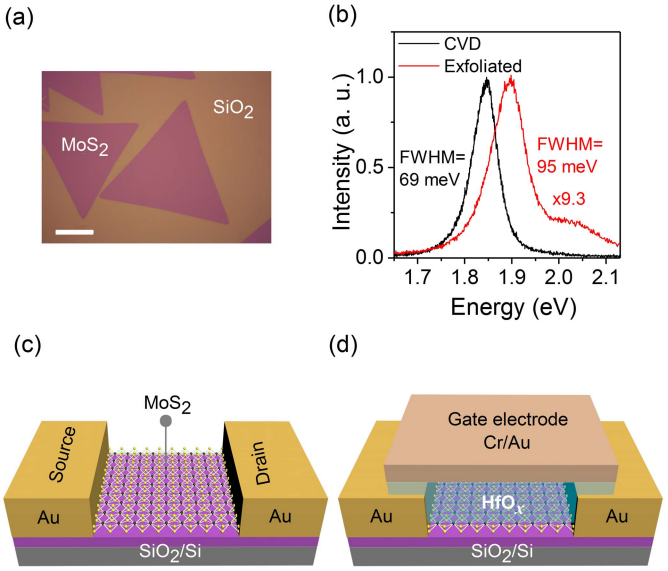

Fig. 1. Fabrication of top-gated transistors from monolayer CVD MoS_2. (a) Optical image of example monolayer CVD flakes. The scale bar is 50 μm. (b) Side-by-side comparison of the PL characteristics of CVD and exfoliated flakes suggests the high quality of our CVD flakes. (c) We formed the source/drain electrodes from Au at about 10^{-8} Torr. (d) Varying the stoichiometric oxygen content of the HfO_x gate dielectric yields device samples with different doping levels. We systematically studied the effects of the dielectric-mediated doping level on the contact resistance and mobility of the top-gated monolayer MoS_2 transistors.

levels. We estimate the doping level in monolayer MoS_2 for those devices using two independent methods: Raman spectroscopy and electrical device measurements, and show that the doping levels estimated using these two methods are consistent. A combination of theoretical modeling and temperature-dependent measurements of our devices with different doping levels reveals two key findings: 1) dielectric-mediated doping reduces the contact resistance by lowering the Schottky barrier height (SBH) and 2) a mixture of the thermionic and field emissions (TFE), even at high carrier densities, dominates the carrier conduction across the metal–MoS_2 interface. Despite the significant improvements in contact resistance by this method, the latter finding points to its potential limitation for achieving ohmic-like contacts in monolayer MoS_2 devices.

II. Device Fabrication

A. Fabrication of Top-Gated MoS_2 Transistors

We made the devices in this paper from monolayer MoS_2 films grown by chemical vapor deposition (CVD). We chose MoS_2 as a model material, because significant knowledge has been generated in literature about its fundamental material and physical properties [19]–[21]. Our CVD process used solid precursors (MoO_3 and sulfur) and was optimized to produce monolayer MoS_2 on heavily doped silicon substrates covered with 285 nm of thermally grown SiO_2. We have described the details of the monolayer TMD growth process from solid precursors in our earlier works [22]–[24]. After the growth, we verified the monolayer thickness of the MoS_2 flakes using a combination of Raman spectroscopy and photoluminescence (PL) measurements. Fig. 1(a) shows an example optical image of our monolayer MoS_2 flakes with dimensions larger than 200 μm. The PL data in Fig. 1(b) suggest the high quality of our monolayer CVD flakes, evident from the narrower linewidth and stronger intensity of the PL response of the CVD flakes than the ones exfoliated from a bulk crystal. Next, we fabricated top-gated transistors from the monolayer CVD MoS_2 flakes.

The device fabrication process starts with defining the active area of the transistors using electron-beam lithography (EBL) followed by patterning in a CF_4:O_2 plasma. We used gold (Au) as the metal electrode for all devices presented in this paper. The Au electrodes were formed through electron-beam (e-beam) evaporation at a high vacuum of about 10^{-8} Torr. Fig. 1(c) shows the device structure after the formation of the source/drain metal electrodes. The above processing steps were identical among all device samples.

Past studies have shown oxygen-vacancy mediated doping of nanomaterials from carbon nanotubes [25] to TMDs [9], [16] using substoichiometric metal oxides, *e.g.*, HfO_x. However, no study has explored the relationship between the chemical composition of the metal oxides and the resulting doping levels in nanomaterials. This information can provide a practical guide for developing a reproducible contact engineering process based on the dielectric-induced doping method. Therefore, we first examined the relationship between the dielectric chemical composition and the level of induced doping in MoS_2 and quantitatively showed that the doping concentration in monolayer MoS_2 increases with reducing the oxygen content of HfO_x (Section II-C). Consequently, this capability allowed us to produce several device samples with different doping levels, which we used to study the effects of doping concentration on the contact resistance and carrier mobility. All devices in our study had ~23-nm-thick HfO_x, formed through an atomic layer deposition (ALD) process at 200 °C. The dielectric constant of the films was measured to be about 12. Forming the top-gate metal electrode through a combination of EBL, e-beam evaporation of Cr/Au, and lift-off completes the fabrication process. Fig. 1(d) shows the schematic of our top-gated MoS_2 transistors.

Next, we thoroughly studied the materials and device characteristics of transistors with four different doping concentrations. To reliably examine the effects of doping on the device metrics, we consistently obtained the materials and device characterization results associated with each doping level from the same MoS_2 transistor. This approach is crucial to avoid possible error in interpreting the results due to device-to-device variations on a given sample.

B. Adjusting Oxygen-Vacancy Mediated Doping Levels in MoS_2

Before we proceed to the device measurement results, we briefly describe our approach for inducing different levels of doping in monolayer CVD MoS_2. We achieved this by tuning the amount of oxygen vacancy in the HfO_x film, *i.e.*, varying x. To do so, we varied the parameters of the oxidation cycles, specifically the wait times, during the thermal

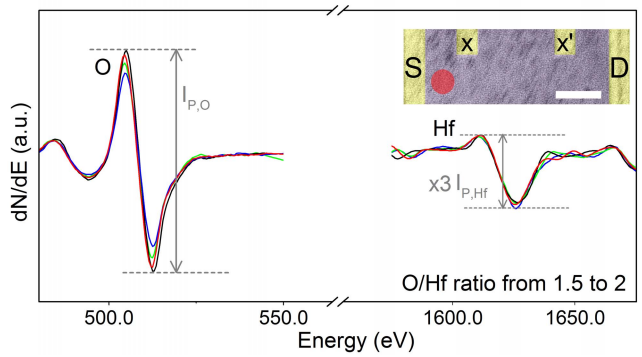

Fig. 2. Measuring HfO_x chemical composition. We used nano-Auger electron spectroscopy to measure locally the chemical composition of the dielectric in the channel region near the source/drain electrodes. Inset: false-colored SEM image of an example device. Red circle: location where the oxygen and hafnium nano-Auger spectra were obtained for this example device. The scale bar is 5 μm. By adjusting the ALD process, we produced four candidate samples with stoichiometric O/Hf ratios of 2.0, 1.9, 1.75, and 1.5.

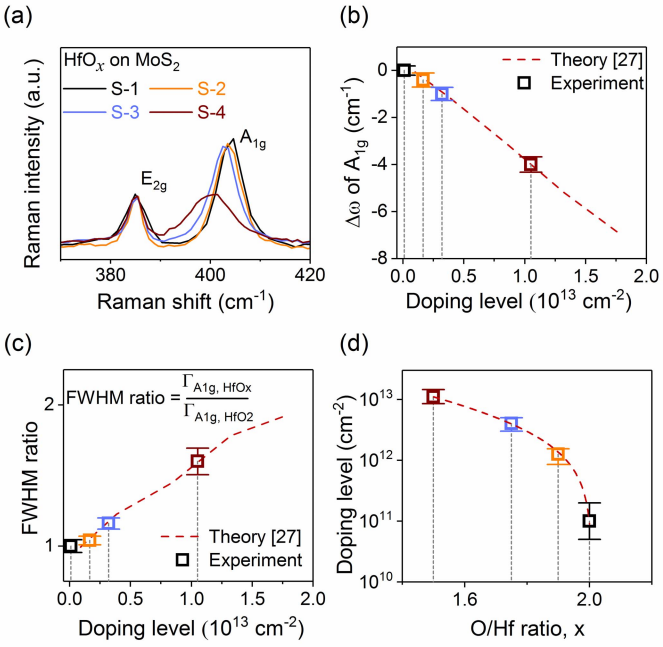

Fig. 3. Estimating dielectric-mediated doping levels in monolayer MoS_2. (a) Typical Raman spectra of the monolayer MoS_2 at regions near the source/drain electrodes for the devices S-1 to S-4. The data indicate the noticeable broadening of the out-of-plane Raman peak accompanied with the change in its peak position with increasing the doping level. (b) and (c) By comparing the experimental Raman data (symbols) and the theoretical predictions (dashed line) from the DFT calculations from [27], we estimated the doping level for those devices. (d) Summary of the estimated doping levels versus the stoichiometric O/Hf ratio. The data illustrate the monotonic increase in the doping level in monolayer MoS_2 with reducing the stoichiometric oxygen content of HfO_x. Dashed line: empirical exponential fit to the experimental data.

ALD of HfO_x. We determined the local chemical composition of the dielectric film in our devices using nano-Auger electron spectroscopy under ultrahigh vacuum of 10^{-10} mbar (Omicron UHV Nanoprobe). Specifically, the small dimension of the Auger measurement window (about 1-μm diameter) together with its integrated low-energy e-beam imaging capability allowed us to accurately probe the chemical composition of the HfO_x dielectric at regions near the source/drain electrodes of our candidate devices. The accurate knowledge of the doping level in the channel regions near the source/drain electrodes is important for revealing its effect on the carrier injection from the contact into the channel. The inset in Fig. 2 shows the top-view scanning electron microscopy (SEM) of an example device after ALD of HfO_x. The red circle in the false-colored SEM image shows the location where the Auger spectra were acquired for this device. Fig. 2 shows the summary of the first derivative of the hafnium and oxygen Auger spectra for four devices. From the data, we then computed the stoichiometric oxygen to hafnium (O/Hf) ratios for each device using the procedure described in [26]. The typical error in the nano-Auger composition measurements is less than 3%. The stoichiometric O/Hf ratios of our candidate devices were 2.0, 1.9, 1.75, and 1.5. From here on, we refer to these devices as S-1, S-2, S-3, and S-4, respectively. Note that in our experiments, we were unable to produce functional devices with x below 1.5. However, as we discuss below, the range of x in our samples provided a sufficiently broad range of doping concentrations, allowing us to quantitatively examine the effects of doping on key device metrics.

C. Raman-Based Estimation of Doping Concentration

Next, we estimated the induced levels of n-type doping in monolayer MoS_2 in relation to the oxygen content of HfO_x. Consistent with the previous reports [9], [16], we observed noticeable changes in the Raman spectra of our candidate devices due to dielectric-mediated doping. Fig. 3(a) illustrates the typical Raman spectra of devices S-1 to S-4 after high-k deposition, where the measurements were made in the channel region near the source/drain electrodes. The broadening of the out-of-plane Raman peak (A_{1g} mode) together with the shift in its peak position qualitatively indicated the monotonic increase in the doping concentration in MoS_2 with reducing the oxygen content of HfO_x. We note that the Raman spectra of these devices were identical before the high-k deposition. Furthermore, the unchanged peak position of the in-plane Raman peak (E_{2g} mode) in these devices after high-k deposition rules out the dielectric-induced strain as a possible cause for the observed changes in A_{1g} modes of the devices. Therefore, we fully attribute the observed changes in the Raman spectra of these devices to dielectric-induced doping by the high-k capping layer.

The theoretical density function theory (DFT) model in [27] predicts the electron charge concentration of monolayer MoS_2 from the full-width-at-half-maximum (FWHM) and the peak location of its out-of-plane Raman peak, represented as dashed lines in Fig. 3(b) and (c). We used this model together with our measured Raman data to estimate the doping level in devices S-1 to S-4. To do so, we fit the out-of-plane Raman peak of each device using a Lorentzian function and extracted its corresponding FWHM and peak location. Next, for each device in our experiments, the estimated doping level was chosen such that it minimizes the sum of squared

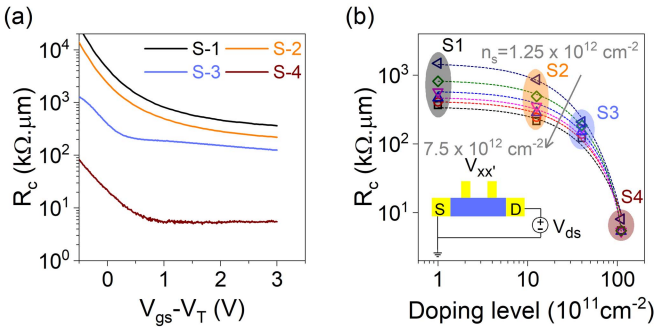

Fig. 4. Effect of doping on the contact resistance. (a) We measured the specific contact resistance R_C of devices S-1 to S-4 using four-point measurements, indicating marked reduction in R_C with increasing the doping level. (b) Scatter plot of R_C versus the doping level as a function of the carrier density. We noticed that the data follow an exponential trend (dashed lines), suggesting the SBH lowering at the metal-MoS_2 interface due to doping. The observed significant reduction in the contact resistance with doping reinforces the finding of the past studies [28]–[32] indicating that the carrier injection from the edge of the contact into the channel in monolayer TMD devices dominates the contact resistance. Inset: schematic of the four-point measurement.

errors compared with the theoretical doping level, predicted by the DFT model, at the measured FWHM and peak location [see Fig. 3(b) and (c)]. Note that the Raman-based doping estimation technique has limited accuracy when determining doping levels below 10^{12} cm^{-2} [as illustrated by the uncertainty in the estimated doping level of device S-1 in Fig. 3(d)].

In Fig. 3(d), we show the plot of the estimated doping concentration versus the stoichiometric oxygen content of HfO_x. The data show that the doping concentration begins to saturate as the stoichiometric O/Hf ratio becomes smaller. These estimated doping levels from the Raman-based method agree with those extracted from the threshold voltage shift of the devices, discussed in Section III-E, confirming the utility of the Raman-based method as a facile approach for estimating doping in monolayer MoS_2.

III. Device Characterization Results

A. Effect of Doping Level on Contact Resistance

We now proceed to examine the effect of dielectric-mediated doping on the device characteristics. Using four-point measurements, see the inset in Fig. 4(b), we first determined the specific contact resistance (R_c) of the S-1 to S-4 devices. We did so by measuring the two-point device conductance ($G_{2pt} = I_d/V_{ds}$), measuring the intrinsic channel conductance ($G_{4pt} = I_d/V_{xx'}$), and then calculating the specific contact resistance using the following expression:

$$2R_c = W\left(\frac{1}{G_{2pt}} - \frac{1}{G_{4pt}} \times \frac{L_{2pt}}{L_{4pt}}\right) \quad (1)$$

where R_c is normalized to the device width (W) and has units of $k\Omega \cdot \mu m$. Fig. 4(a) shows the plot of R_c *versus* the gate overdrive voltage ($V_{gs} - V_T$) for the S-1 to S-4 devices. Here, V_{gs} and V_T denote the gate–source and threshold voltages, respectively. The data indicated over two orders of magnitude reduction in the specific contact resistance due to the increase in the doping level. In top-gated monolayer TMD transistors, the carrier injection from the contact into the channel dominates the contact resistance [28]–[32], where the level of injection depends only on the width and height of the Schottky barrier. Therefore, we hypothesized that the dielectric-mediated doping reduces the contact resistance by lowering the SBH, which also narrows the barrier simultaneously, at the edge of the contact. This hypothesis, therefore, predicts that the device current at the flatband, which depends only on SBH, increases with increasing the doping level (discussed in Section III-B).

To gain more insights into the effect of doping on the contact resistance, we then made the scatter plot of R_c versus the doping level as a function of the carrier density (n_s), shown in Fig. 4(b). The high series resistance in TMD-based devices prevents the direct extraction of mobile charges in the channel using Hall measurements [14]. Alternatively, we estimated the carrier density at a given gate overdrive voltage using

$$n_s = \frac{C_{ox}(V_{gs} - V_T)}{q} \quad (2)$$

where C_{ox} and q are the oxide capacitance per unit area and the elementary charge, respectively. We made two key observations from the plot in Fig. 4(b). First, the dependence of R_c on the density of charge carrier in the channel becomes weaker with increasing the doping level in MoS_2. Second, the contact resistance appears to exponentially decay with increasing the MoS_2 doping level at the edge of the contacts. This observation suggests that the dielectric-mediated doping reduces the SBH at the edge of the contact, which is consistent with our hypothesis. To verify this, we next examined the effect of the channel doping on the SBH at the metal–MoS_2 interface for devices S-1 to S-4.

B. Effect of Dielectric-Mediated Doping on SBH

Previous studies have shown the utility of temperature-dependent measurements for extracting SBH in devices made from multilayer TMDs [5], [33]. However, a recent study by Kim *et al.* [34] suggests that extra care must be taken for measuring SBH in monolayer MoS_2 devices using temperature-dependent measurements. Specifically, they show that using low-temperature (293–173 K) measurement data can grossly underestimate the SBH of monolayer MoS_2 transistors, whereas the high-temperature (373–473 K) device data yield a more reliable measure of SBH. In our experiments, we noticed that the low-temperature (300–100 K) characteristics of the S-1 to S-4 devices give a similar SBH of about 70 meV, regardless of the doping level (data not shown). Considering the noticeably different current density at about the flat-band voltage (V_{FB}) of these devices, shown in Fig. 5, we conclude that the extracted SBH from the low-temperature measurements are possibly incorrect. On the other hand, we were unable to extract the SBH by measuring the device characteristics at elevated temperatures due to the breakdown of the gate dielectric. Therefore, we used an alternative method, described next, for estimating the SBH of our devices.

To estimate the SBH of the S-1 to S-4 devices, we used the modeling framework proposed by Appenzeller *et al.* [30]. This approach is based on two properties of Schottky barrier transistors: 1) the drain current at the gate voltages below

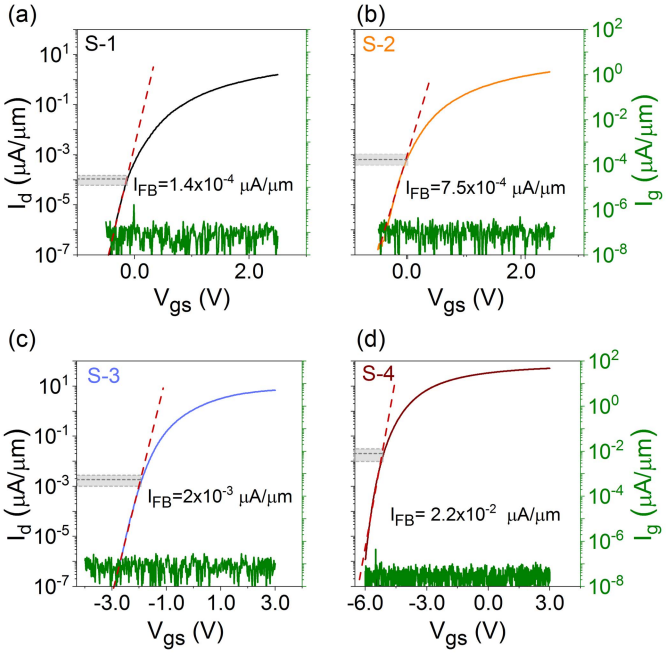

Fig. 5. Identifying the current and voltage at the flat-band condition. Transfer characteristics of (a) S-1, (b) S-2, (c) S-3, and (d) S-4 devices, measured at V_{ds} = 1 V. Dashed red line: expected exponential trend of the device characteristics in the subthreshold regime. We identify the point at which the device characteristics begin to deviate from this exponential trend as the flat-band. The data clearly show that the current at the flat-band, I_{FB}, increases with increasing the doping. We used I_{FB} to determine the SBH of these devices. The gray band in each plot represents the uncertainty in identifying I_{FB}. In these plots, we also show the corresponding gate leakage I_g for each device, which is within the measurable limit of our instrument. All devices had a gate width of 15 μm.

V_{FB} is due to the thermionic emission of charge carriers over the energy barrier between the metal and the semiconductor, *i.e.*, it depends only on SBH and (2) the energy barrier at V_{FB} represents the true SBH (ϕ_n) at the metal–semiconductor interface [5]. Next, we calculated the theoretical current at the flat-band condition (I_{FB}) as a function of ϕ_n using

$$I_{FB} = q \int_{\phi_n}^{\infty} M(E - \phi_n) f(E) dE \tag{3}$$

where $f(E)$ is the Fermi–Dirac distribution function. In this expression, $M(E)$ gives the number of modes per unit width in the 2-D channel using

$$M(E) = \frac{2}{h^2} \sqrt{2m_e^* E} \tag{4}$$

where h is Planck's constant and m_e^* is the electron effective mass in monolayer MoS_2. In our calculations, we assumed an effective electron mass of 0.46 m_0, where m_0 is the electron mass. We then found the experimental I_{FB} for devices S-1 to S-4. We did so by first identifying the point in the subthreshold region of the device transfer characteristics where the curve begins to deviate from the exponential trend (the dashed red lines in Fig. 5). The gray band in each plot represents the level of uncertainty in identifying I_{FB}, and hence the error in estimating SBH using this method. Note the increase in I_{FB} with the doping level, which is consistent with the prediction of our hypothesis that SBH at the edge of

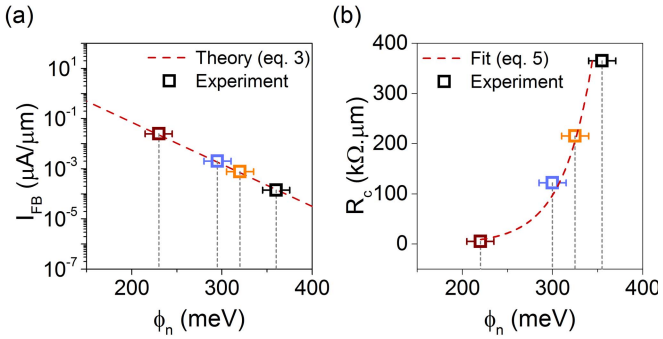

Fig. 6. Extraction of SBH. (a) We found SBH for our devices S-1 to S-4 by comparing the experimental I_{FB} from Fig. 5 (symbols) with the theoretical predictions from Eq. 3 (dashed line). The data show that the SBH decreases with increasing the doping level. (b) Plot of R_c versus ϕ_n, indicating a marked reduction of the contact resistance with increasing doping. Dashed line: exponential fit using Eq. 5, suggesting that the carrier injection at the contact is dominated by a mixture of TFE.

the contact decreases with increasing the dielectric-mediated doping.

Next, we extracted ϕ_n for the S-1 to S-4 devices by comparing the experimental I_{FB} with the theoretical data from Eq. 3. Fig. 6(a) Summary of this method for extracting ϕ_n from the experimental and theoretical I_{FB}. The error bars for ϕ_n were calculated from the upper and lower bounds of I_{FB}, represented by the gray bands in Fig. 5. From the data, we made two key observations. First, the extracted true SBH for the device S-1 (lowest doping) is about 350 meV, which agrees with the measured true SBH of Au on monolayer MoS_2 reported by Kim *et al.* [34]. Second, the dielectric-mediated doping reduces the true SBH at the metal–MoS_2 interface; this is an important finding pertaining to the effect of doping on SBH. This finding explains the observed drastic improvement of R_c with increasing the doping level in our devices (see Fig. 4).

Having established the effect of doping on the SBH, we next examined the carrier conduction mechanism across the metal–MoS_2 interface when the carrier density in the channel is high. Therefore, we plotted the R_c data for the devices S-1 to S-4 versus their corresponding ϕ_n at the carrier density of 7.5 $\times$ 10^{12} cm^{-2}, as shown in Fig. 6(b). We then used the following exponential function to fit the experimental data:

$$R_c = A \times \exp\left(\frac{q\phi_n}{E_{00} \cdot \coth(E_{00}/kT)}\right) \tag{5}$$

where A and E_{00} are the fitting parameters and kT denotes the thermal energy, which has units of eV. We found that this function with E_{00} of about 24 meV provides a reasonable fit to the experimental data, suggesting that the conduction mechanism of carriers across the contact is a mixture of TFE [35]. We note that other exponential functions, describing the conduction due to a single source (either thermionic emission or field emission), did not fit our experimental results in Fig. 6(b). To support this conclusion, we next investigated the temperature dependence of the contact resistance for the devices S-1 to S-4.

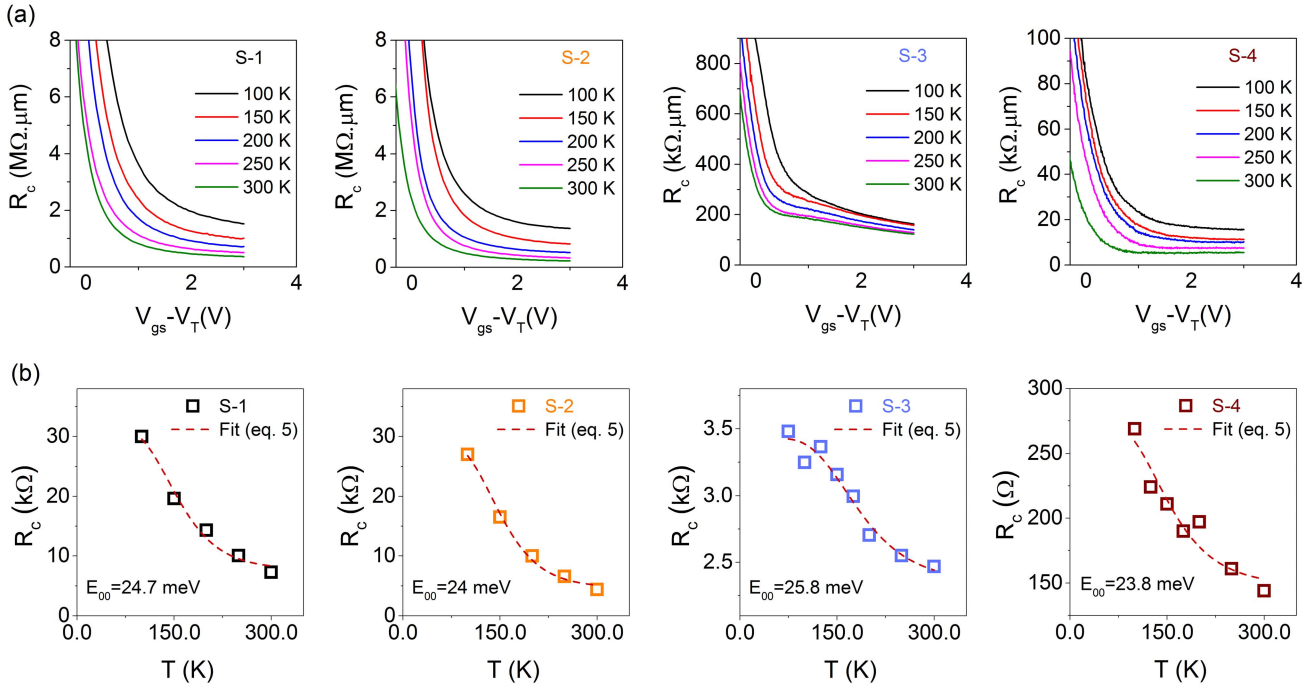

Fig. 7. Temperature-dependent measurements of contact resistance. (a) Plots of R_C versus the gate overdrive voltage as a function of temperature for the devices S-1 to S-4. The resistance increases with reducing temperature, suggesting a barrier-limited behavior. (b) Temperature-dependent plots of R_C at the carrier density of 7.5 $\times$ 10^{12} cm^{-2}. The fit using Eq. 5 confirms that the carrier injection at the contact is a mixture of TFE. This finding points to the limitation of the dielectric-mediated doping for reducing the contact resistance. Further reduction of SBH using alternative methods is necessary to obtain ohmic-like contacts to monolayer MoS_2.

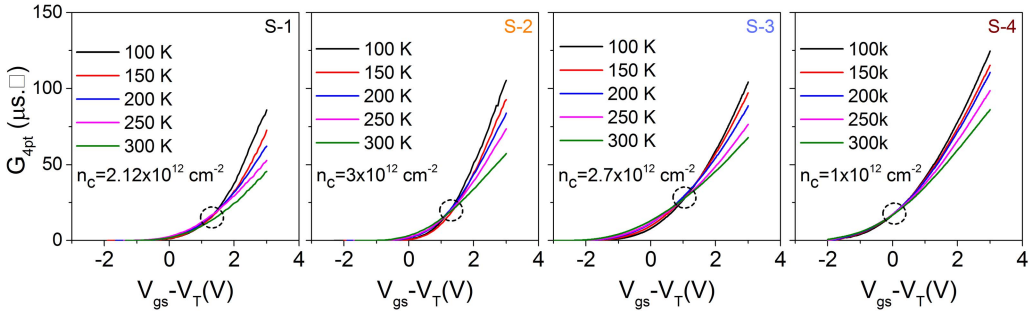

Fig. 8. Effect of dielectric-mediated doping on carrier transport. Temperature-dependent plots of the intrinsic channel conductance as a function of the gate overdrive voltage for the devices S-1 to S-4. Our device samples exhibit a metal-to-insulator crossover at a carrier density n_c of 1–3 $\times$ 10^{12} cm^{-2}.

C. Temperature Dependence of Contact Resistance

To gain further insight into the factors limiting the specific contact resistance of the monolayer MoS_2 transistors, we performed temperature-dependent measurements (100–300 K) on our candidate devices, S-1 to S-4. Fig. 7(a) shows the summary plots of R_c versus the gate overdrive voltage as a function of temperature. In this temperature range, the data show that the contact resistance for all devices (S-1 to S-4) increased with reducing temperature, indicating a barrier-limited behavior. In Fig. 7(b), we then plotted the variations of R_c as a function of temperature at the carrier density of 7.5 $\times$ 10^{12} cm^{-2}. We found that only Eq. 5 can provide a reasonable fit to the temperature-dependent R_c data of S-1 to S-4 devices, giving an E_{00} of about 23–26 meV. To perform these curve fittings, we kept ϕ_n fixed for each device sample and used its corresponding value from Fig. 6(a). The temperature-dependent characteristics of R_c confirms that the conduction mechanism of carrier across the contact is TFE.

D. Effect of Doping on Carrier Mobility

While we demonstrated in the previous sections that the dielectric-mediated doping improves the contact resistance, it is important to investigate its effect on another key device metric, carrier mobility. In particular, to determine the dominant carrier scattering mechanism in the channel, we performed temperature-dependent transport measurements. Fig. 8 shows the temperature-dependent measurements of the four-point channel conductance (G_{4pt}) as a function of the gate overdrive voltage for the S-1 to S-4 devices. The data illustrate a disorder-driven crossover to insulating behavior at

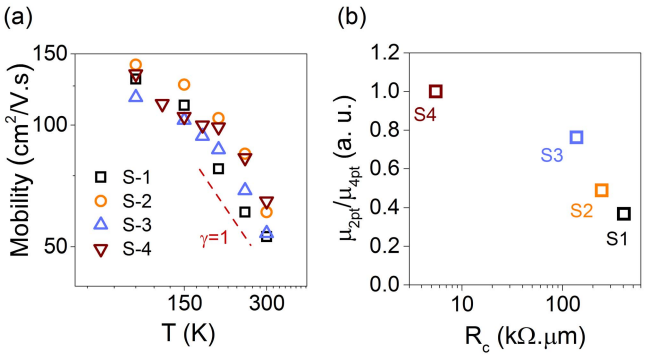

Fig. 9. Temperature-dependent measurements of mobility. (a) Variation of carrier mobility as a function of temperature, suggesting that acoustic phonon scattering is the main mobility limiting factor in the metallic regime at temperatures above 200 K. (b) Ratio of the two-point-to-four-point mobility (μ_{2pt}/μ_{4pt}) for each device. The results for the two mobility calculations begin to converge as the contact resistance becomes smaller.

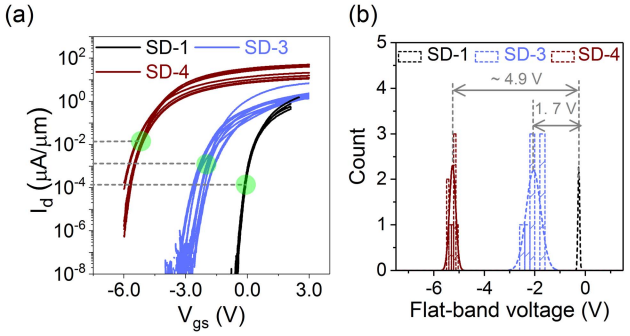

Fig. 10. Electrical measurements of doping level. (a) Shift in the flat-band voltage provides a measure of doping in the channel according to Eq. 8. Transfer characteristics of multiple devices on the samples SD-1, SD-3, and SD-4. We note that devices on a given sample have different channel lengths, resulting in the observed variations in the ON current. The current in the OFF-state is however invariant to the channel length. We identified the flat-band voltages (the green circles) for the different devices using the method explained in Fig. 5. (b) Distribution plots of the flat-band voltage for the samples SD-1, SD-3, and SD-4. Since the doping level of SD-1 is considerably lower than the other device samples, and hence by using its flat-band voltage as the reference, we estimated a doping concentration of about 4.5×10^{12} and 1.2×10^{13} cm^{-2} for the samples SD-3 and SD-4. These values agree with the doping levels estimated from the Raman data in Fig. 3.

low carrier densities ($n_c \sim 1$–3×10^{12} cm^{-2}) for all devices. Beyond this point, G_{4pt} increases with decreasing temperature, indicating a metallic transport. We then calculated the four-point mobility μ_{4pt} of each device in the metallic regime using

$$\mu_{4pt} = \frac{1}{C_{ox}} \frac{L_{4pt}}{W} \frac{dG_{4pt}}{dV_{gs}}. \tag{6}$$

Fig. 9(a) shows the variation of μ_{4pt} versus temperature in the metallic regime for the S-1 to S-4 devices. The data clearly show that the carrier mobility of these devices are in the same range, ~50–65 cm$^2 \cdot$ V$^{-1} \cdot$ s^{-1} at room temperature. Furthermore, the variation of μ_{4pt} follows a power-law dependence, $\mu_{4pt} \propto T^{-\gamma}$, with γ of about 1 at temperatures above 200 K. The values of γ in this temperature range suggest that acoustic phonon is the dominant scattering mechanism in these devices [36]. From the temperature-dependent transport measurements, we make two conclusions. First, our dielectric-mediated doping process does not alter the mobility-limiting scattering mechanism in the channel. The second conclusion stems from the observed equivalency of the intrinsic mobility in these devices. Therefore, we fully attribute the marked reduction of R_c to the doping-induced SBH lowering at the metal–MoS_2 interface.

We also calculated the two-point mobility, μ_{2pt}, of the S-1 to S-4 devices. This mobility represents the field-effect mobility of the device and is calculated using

$$\mu_{2pt} = \frac{1}{C_{ox}} \frac{L_{2pt}}{W} \frac{dG_{2pt}}{dV_{gs}}. \tag{7}$$

In Fig. 9(b), we show the ratio of μ_{2pt} to μ_{4pt} for each device. Consistent with the previous reports [37], this plot clearly shows that the high contact resistance of devices can lead to gross underestimation of the mobility. However, the consistency of the two-point and four-point mobility calculation results improves as the contact resistance becomes smaller, *e.g.*, device S-4.

E. Effect of Doping on the Device Threshold Voltage

In Section II-C, we described the utility of Raman spectroscopy for estimating the doping level in monolayer MoS_2. The shift in the flat-band voltage, or equivalently the threshold voltage, can also provide quantitative information about the amount of fixed charges in the oxide, and hence the doping level in the semiconductor using the following equation:

$$\Delta N_D = N_{D,i} - N_{D,j} = \frac{C_{ox}|V_{FB,i} - V_{FB,j}|}{q} \tag{8}$$

where $N_{D,i}$ and $N_{D,j}$ denote the doping level in device samples i and j, respectively. To determine the doping level from the electrical measurements, we first identified V_{FB} of the sister devices to S-1 to S-4 transistors, *i.e.*, devices that were on the same sample with each of those devices. We refer to those samples SD-1 to SD-4, correspondingly. To determine V_{FB} of devices on SD-1 to SD-4 samples, we use the method described in Fig. 5 in Section III-B. Fig. 10(a) shows the transfer characteristics of multiple devices on samples SD-1, SD-3, and SD-4. In this plot, we do not show the data for SD-2, because they are mostly overlapping with those of SD-1. The reason for the overlap stems from the small difference in the V_{FB} of SD-1 and SD-2 on the one hand, and the relatively large variations of V_{FB} among devices on the same sample on the other hand. In addition, we note that the variations of the ON current among devices on a given sample in Fig. 10(a) mostly originates from the difference in their channel lengths. However, I_{FB} is invariant to the channel length, assuming that in the OFF-state, scattering in the channel is negligible. Therefore, using the flat-band current provides a reliable measure for finding the distribution of V_{FB} for these samples. In Fig. 10(b), we show the distribution of V_{FB} for the samples SD-1, SD-3, and SD-4. Assuming that SD-1 has

significantly lower doping level than the other samples, and hence by using its V_{FB} as the reference in Eq. 8, we obtained a doping concentration of about 4.5×10^{12} and 1.2×10^{13} cm^{-2} for the device samples SD-3 and SD-4, respectively. These values of the doping level for the samples SD-3 and SD-4 agree with those obtained based on the Raman analysis in Fig. 3, highlighting the utility of the Raman spectroscopy as a simple method for estimating dielectric-mediated doping in monolayer MoS_2.

IV. Conclusion

In summary, we systematically investigated the effects of dielectric-mediated doping on the electrical properties of devices made from monolayer MoS_2. Our results presented here establish several key findings. First, our results illustrate the utility of Raman spectroscopy as a noninvasive and facile approach for estimating dielectric-mediated doping levels in monolayer MoS_2. The Raman-based estimation method is however more reliable when dealing with doping levels higher than 10^{12} cm^{-2}. Second, our electrical measurements of devices with different doping levels reveal that the dielectric-mediated doping of the channel regions in the vicinity of the contact electrodes is effective in reducing the SBH. Third, the observed drastic reduction in the contact resistance in this paper (over two orders of magnitude) by increasing the doping level reinforces the findings of the recent experimental and theoretical studies [28]–[30], [32] suggesting that the carrier injection in top-gated monolayer TMD devices occurs mostly from the edge of the contacts. Finally, despite the effectiveness of the doping-mediated method in lowering the SBH, the temperature-dependent measurements revealed that the carrier injection into the channel in those devices remains a mixture of TFE, even for the device with a doping level as high as 1.5×10^{13} cm^{-2}. Therefore, further reduction of the barrier height by complementing the dielectric-mediated doping technique with other methods (*e.g.*, work function engineering) is necessary for achieving ohmic-like contacts in TMD-based devices.

Acknowledgment

The authors would like to thank S. Tenney of the Brookhaven National Laboratory for the helpful discussions and assistance with the nano-Auger measurements. The device fabrication was performed in part at the NanoFabrication Facility of the CUNY Advanced Science Research Center.

References

[1] J. K. Ellis, M. J. Lucero, and G. E. Scuseria, "The indirect to direct band gap transition in multilayered MoS_2 as predicted by screened hybrid density functional theory," *Appl. Phys. Lett.*, vol. 99, no. 26, p. 261908, 2011.

[2] X. Fan, D. J. Singh, and W. Zheng, "Valence band splitting on multilayer MoS_2: Mixing of spin–orbit coupling and interlayer coupling," *J. Phys. Chem. Lett.*, vol. 7, no. 12, pp. 2175–2181, 2016.

[3] A. Chernikov *et al.*, "Electrical tuning of exciton binding energies in monolayer WS_2," *Phys. Rev. Lett.*, vol. 115, p. 126802, Sep. 2015.

[4] D. Shahrjerdi, A. D. Franklin, S. Oida, J. A. Ott, G. S. Tulevski, and W. Haensch, "High-performance air-stable n-type carbon nanotube transistors with erbium contacts," *ACS Nano*, vol. 7, no. 9, pp. 8303–8308, 2013.

[5] S. Das, H.-Y. Chen, A. V. Penumatcha, and J. Appenzeller, "High performance multilayer MoS_2 transistors with scandium contacts," *Nano Lett.*, vol. 13, no. 1, pp. 100–105, 2012.

[6] X. Cui *et al.*, "Multi-terminal transport measurements of MoS_2 using a van der Waals heterostructure device platform," *Nature Nanotechnol.*, vol. 10, no. 6, pp. 534–540, 2015.

[7] R. Kappera *et al.*, "Phase-engineered low-resistance contacts for ultrathin MoS_2 transistors," *Nature Mater.*, vol. 13, pp. 1128–1134, Sep. 2014.

[8] L. Yang *et al.*, "Chloride molecular doping technique on 2D materials: WS_2 and MoS_2," *Nano Lett.*, vol. 14, no. 11, pp. 6275–6280, 2014.

[9] A. Rai *et al.*, "Air stable doping and intrinsic mobility enhancement in monolayer molybdenum disulfide by amorphous titanium suboxide encapsulation," *Nano Lett.*, vol. 15, no. 7, pp. 4329–4336, 2015.

[10] M. R. Müller *et al.*, "Gate-controlled WSe_2 transistors using a buried triple-gate structure," *Nanoscale Res. Lett.*, vol. 11, no. 1, p. 512, 2016.

[11] A. Valsaraj, J. Chang, A. Rai, L. F. Register, and S. K. Banerjee, "Theoretical and experimental investigation of vacancy-based doping of monolayer MoS_2 on oxide," *2D Mater.*, vol. 2, no. 4, p. 045009, 2015.

[12] J. Wang *et al.*, "High mobility MoS_2 transistor with low Schottky barrier contact by using atomic thick h-BN as a tunneling layer," *Adv. Mater.*, vol. 28, no. 37, pp. 8302–8308, 2016.

[13] A. Avsar *et al.*, "Van der waals bonded Co/h-BN contacts to ultrathin black phosphorus devices," *Nano Lett.*, vol. 17, no. 9, pp. 5361–5367, 2017.

[14] X. Cui *et al.*, "Low-temperature ohmic contact to monolayer MoS_2 by van der Waals bonded Co/h-BN electrodes," *Nano Lett.*, vol. 17, no. 8, pp. 4781–4786, 2017.

[15] C. D. English, G. Shine, V. E. Dorgan, K. C. Saraswat, and E. Pop, "Correction to improved contacts to MoS_2 transistors by ultra-high vacuum metal deposition," *Nano Lett.*, vol. 17, no. 4, p. 2739, 2017.

[16] A. Sanne *et al.*, "Radio frequency transistors and circuits based on CVD MoS_2," *Nano Lett.*, vol. 15, no. 8, pp. 5039–5045, Jul. 2015.

[17] A. Rai *et al.*, "Interfacial-oxygen-vacancy mediated doping of MoS_2 by high-*k* dielectrics," in *Proc. 73rd Annu. Device Res. Conf. (DRC)*, Jun. 2015, pp. 189–190.

[18] C. J. Mcclellan, E. Yalon, K. K. H. Smithe, S. V. Suryavanshi, and E. Pop, "Effective n-type doping of monolayer MoS_2 by AlO_x," in *Proc. 75th Annu. Device Res. Conf. (DRC)*, Jun. 2017, pp. 1–2.

[19] K. F. Mak, C. Lee, J. Hone, J. Shan, and T. F. Heinz, "Atomically thin MoS_2: A new direct-gap semiconductor," *Phys. Rev. Lett.*, vol. 105, p. 136805, Sep. 2010.

[20] A. Splendiani *et al.*, "Emerging photoluminescence in monolayer MoS_2," *Nano Lett.*, vol. 10, no. 4, pp. 1271–1275, Mar. 2010.

[21] Q. H. Wang, K. Kalantar-Zadeh, A. Kis, J. N. Coleman, and M. S. Strano, "Electronics and optoelectronics of two-dimensional transition metal dichalcogenides," *Nature Nanotechnol.*, vol. 7, no. 11, pp. 699–712, Nov. 2012.

[22] A. Alharbi, P. Zahl, and D. Shahrjerdi, "Material and device properties of superacid-treated monolayer molybdenum disulfide," *Appl. Phys. Lett.*, vol. 110, no. 3, p. 033503, 2017.

[23] A. Alharbi, D. Armstrong, S. Alharbi, and D. Shahrjerdi, "Physically unclonable cryptographic primitives by chemical vapor deposition of layered MoS_2," *ACS Nano*, vol. 11, no. 12, pp. 12772–12779, 2017.

[24] A. Alharbi and D. Shahrjerdi, "Electronic properties of monolayer tungsten disulfide grown by chemical vapor deposition," *Appl. Phys. Lett.*, vol. 109, no. 19, p. 193502, 2016.

[25] N. Moriyama, Y. Ohno, T. Kitamura, S. Kishimoto, and T. Mizutani, "Change in carrier type in high-*k* gate carbon nanotube field-effect transistors by interface fixed charges," *Nanotechnology*, vol. 21, no. 16, p. 165201, 2010.

[26] K. D. Childs and C. L. Hedberg, *Handbook of Auger Electron Spectroscopy: A Book of Reference Data for Identification and Interpretation in Auger Electron Spectroscopy*. Eden Prairie, MN, USA: Physical Electronics Inc., 1995.

[27] B. Chakraborty, A. Bera, D. V. S. Muthu, S. Bhowmick, U. V. Waghmare, and A. K. Sood, "Symmetry-dependent phonon renormalization in monolayer MoS_2transistor," *Phys. Rev. B, Condens. Matter*, vol. 85, p. 161403(R), Apr. 2012.

[28] G. Arutchelvan *et al.*, "From the metal to the channel: A study of carrier injection through the metal/2D MoS_2 interface," *Nanoscale*, vol. 9, no. 30, pp. 10869–10879, 2017.

[29] A. Prakash, H. Ilatikhameneh, P. Wu, and J. Appenzeller, "Understanding contact gating in Schottky barrier transistors from 2D channels," *Sci. Rep.*, vol. 7, Oct. 2017, Art. no. 12596.
[30] J. Appenzeller, F. Zhang, S. Das, and J. Knoch, "Transition metal dichalcogenide Schottky barrier transistors: A device analysis and material comparison," *2D Mater. Nanoelectron.*, vol. 17, pp. 207–240, May 2016.
[31] D. S. Schulman, A. J. Arnold, and S. Das, "Contact engineering for 2D materials and devices," *Chem. Soc. Rev.*, vol. 47, no. 9, pp. 3037–3058, 2018.
[32] R. Grassi, Y. Wu, S. J. Koester, and T. Low, "Semianalytical model of the contact resistance in two-dimensional semiconductors," *Phys. Rev. B, Condens. Matter*, vol. 96, p. 165439, Oct. 2017.
[33] A. Allain, J. Kang, K. Banerjee, and A. Kis, "Electrical contacts to two-dimensional semiconductors," *Nature Mater.*, vol. 14, no. 12, pp. 1195–1205, 2015.
[34] C. Kim *et al.*, "Fermi level pinning at electrical metal contacts of monolayer molybdenum dichalcogenides," *ACS Nano*, vol. 11, no. 2, pp. 1588–1596, 2017.
[35] K. K. Ng and S. M. Sze, *Physics of Semiconductor Devices*, 3rd ed. Hoboken, NJ, USA: Wiley, 2006.
[36] H. C. P. Movva *et al.*, "High-mobility holes in dual-gated WSe_2 field-effect transistors," *ACS Nano*, vol. 9, no. 10, pp. 10402–10410, 2015.
[37] S. Larentis, B. Fallahazad, and E. Tutuc, "Field-effect transistors and intrinsic mobility in ultra-thin $MoSe_2$ layers," *Appl. Phys. Lett.*, vol. 101, no. 22, p. 223104, 2012.

Abdullah Alharbi (M'09) received the B.S. degree in electrical engineering (EE) from King Abdulaziz University, Jeddah, Saudi Arabia, and the M.S. degree in EE from New York University, Brooklyn, NY, USA, where he is currently pursuing the Ph.D. degree.

His current research interests include device engineering and physics of 2-D materials.

Davood Shahrjerdi (SM'16) received the Ph.D. degree in solid-state electronics from The University of Texas at Austin, Austin, TX, USA.

He is currently an Assistant Professor of electrical and computer engineering with New York University, Brooklyn, NY, USA. His current research interests include the science and technology of emerging nanomaterials and devices and their interfaces with silicon CMOS.